Received: 30 June 2021 | Revised: 8 April 2022 | Accepted: 13 April 2022

DOI: 10.1002/cne.25332

RESEARCH ARTICLE

JCN RESEARCH IN SYSTEMS NEUROSCIENCE THE JOURNAL OF COMPARATIVE NEUROLOGY WILEY

Topographic organization underlies intrinsic and morphological heterogeneity of central amygdala neurons expressing corticotropin-releasing hormone

Jun-Nan Li[1,2,3] | **Kevin Chen**[1,3,4] | **Patrick L. Sheets**[1,3]

[1]Department of Pharmacology and Toxicology, Indiana University School of Medicine, Indianapolis, Indiana, USA

[2]Department of Anesthesiology, Washington University Pain Center, Washington University School of Medicine in St. Louis, St. Louis, MO 63110, USA

[3]Stark Neurosciences Research Institute, Indiana University School of Medicine, Indianapolis, Indiana, USA

[4]Zionsville Community High School, Zionsville, Indiana, USA

Correspondence
Patrick L. Sheets, Stark Neurosciences Research Institute, Indiana University School of Medicine, Neuroscience Research Building 400D, 320 West 15th St, Indianapolis, IN 46202, USA.
Email: plsheets@iu.edu

Present address
Jun-Nan Li, Department of Anesthesiology, Washington University Pain Center, Washington University School of Medicine in St. Louis, St. Louis, MO 63110, USA

Funding information
NIH, Grant/Award Number: R01-NS112632

Abstract

The central nucleus of the amygdala (CeA) network consists of a heterogeneous population of inhibitory GABAergic neurons distributed across distinct subregions. While the specific roles for molecularly defined CeA neurons have been extensively studied, our understanding of functional heterogeneity within classes of molecularly distinct CeA neurons remains incomplete. In addition, manipulation of genetically defined CeA neurons has produced inconsistent behavioral results potentially due to broad targeting across CeA subregions. Therefore, elucidating heterogeneity within molecularly defined neurons in subdivisions of the CeA is pivotal for gaining a complete understanding of how CeA circuits function. Here, we used a multifaceted approach involving transgenic reporter mice, brain slice electrophysiology, and neuronal morphology to dissect the heterogeneity of corticotropin-releasing hormone (CRH) neurons in topographically distinct subregions of the CeA. Our results revealed that intrinsic and morphological properties of CRH-expressing (CRH+) neurons in the lateral (CeL) and medial (CeM) subdivisions of the CeA were significantly different. We found that CeL-CRH+ neurons are relatively homogeneous in morphology and firing profile. Conversely, CeM-CRH+ neurons displayed heterogeneous electrophysiological and morphological phenotypes. Overall, these results show phenotypic differences between CRH+ neurons in CeL and CeM.

KEYWORDS
central amygdala, corticotropin-releasing hormone, intrinsic properties, morphology, topography

1 | INTRODUCTION

The amygdala is the almond-shaped limbic structure involved in emotionally laden memories and pain affect. The amygdala is commonly and broadly divided into the basolateral complex (BLA; the primary sensory input zone of the amygdala) and the central amygdala (CeA; the major output structure of the amygdala) (Janak & Tye, 2015; Marek et al., 2013; Neugebauer et al., 2004; Pape & Pare, 2010; Thompson & Neugebauer, 2017). The CeA sends robust projections to the hypothalamus and brain stem, which are regions important for controlling innate behaviors, and the acquisition, consolidation, and expression of conditioned behaviors (Fadok et al., 2018; Keifer Jr. et al., 2015). The CeA receives nociceptive sensory information from the spinal cord and brain stem via the parabrachial nucleus (PBn) and multimodal information (including nociceptive sensory information) via the thalamus comprising a key circuit involved in aversive and emotional

aspects of pain (Bernard et al., 1996, 1993; Chiang et al., 2020; Fulwiler & Saper, 1984; Gauriau & Bernard, 2002; Jhamandas et al., 1996; Li & Sheets, 2020; Nagase et al., 2019; Neugebauer, 2015; Saper & Loewy, 1980; Sarhan et al., 2005; Tokita et al., 2010). The CeA contains anatomically and functionally distinct subregions denoted the central lateral capsular (CeC), the central lateral (CeL), and the central medial (CeM) amygdala. These CeA subregions form a highly complex network of topographically organized connections (Duvarci & Pare, 2014; Fadok et al., 2018; Jolkkonen & Pitkanen, 1998; Keifer Jr. et al., 2015; Kim et al., 2017; McCullough et al., 2018).

Corticotropin-releasing hormone (CRH), primarily released from hypothalamic paraventricular nucleus (PVN) neurons, is the major component of the hypothalamic–pituitary–adrenocortical (HPA axis) stress response (Herman et al., 2011). However, CRH is also expressed in the CeA (Joseph & Knigge, 1983), which contains the highest expression of CRH-producing cells outside of the hypothalamus (Callahan et al., 2013). One study showed that CRH was primarily expressed in CeL neurons (69.9% ± 3.8%) with smaller populations in CeM (20.7% ± 5.1%) and sparse expression in CeC (9.4% ± 4.1%) (McCullough et al., 2018). It has been demonstrated that CRH+ neurons in the CeA are critical for discriminative fear but are not required for generalized fear (Sanford et al., 2017). This same work also reported that most CRH+ neurons in the CeA send projections locally with only a few having long-range projections (Sanford et al., 2017). Another study showed that CRH+ neurons in the CeA can control rapid selection of passive or active defensive behaviors via recurrent inhibitory interactions with somatostatin-expressing (SOM+) neurons (Fadok et al., 2017). These findings suggest that CRH+ neurons within the CeA function mainly as a local circuit.

Other studies show that CRH+ neurons send projections out of the CeA and play critical roles in specific behaviors. For example, activation of CeA-CRH+ neurons projecting to the bed nucleus of the stria terminalis (BNST) drive excessive alcohol drinking and withdrawal in dependent rats (de Guglielmo et al., 2019). These same BNST-projecting CeA-CRH+ neurons have also been shown to mediate anxiety behavior (Pomrenze, Tovar-Diaz, et al., 2019). Silencing of CeA-CRH+ neurons consolidated specific components of fear memory (Asok et al., 2018). Overall, these results show that CeA-CRH+ neurons are functionally diverse population of neurons. However, the homogeneity/heterogeneity of the CRH+ neurons within and across subregions of the CeA has not fully elucidated. In this study, we aimed to define physiological and morphological identities for CeA-CRH+ neuron using transgenic markers, slice electrophysiology, and confocal imaging.

2 | METHODS

2.1 | Animals

To visualize CeA neurons expressing CRH, female homozygous CRH-ires-Cre mice (Jackson Laboratories: Stock no. 013044) were mated with male homozygous Ai14 mice (Jackson Laboratories: Stock no. 007914) to obtain litters of CRH-ires-Cre;Ai14 mice (CRH-TdTomato mice). Offspring of both sexes were used in all experiments. Mice were housed on a 12:12 h light:dark schedule (lights on at 7:00 a.m.) with ad libitum access to food and water.

2.2 | Acute brain slice preparation

After brief anesthetization by isoflurane, mice were decapitated and brains were rapidly extracted (<1 min) and placed in ice-chilled cutting solution (in mM: 110 choline chloride, 25 $NaHCO_3$ [sodium bicarbonate], 25 D-glucose, 11.6 sodium ascorbate, 7 $MgSO_4$ [magnesium sulfate], 3.1 sodium pyruvate, 2.5 KCl, 1.25 NaH_2PO_4, and 0.5 $CaCl_2$). Coronal slices (300 μm) containing the amygdala were prepared by vibratome (VT1200S, Leica), and transferred to artificial cerebrospinal solution (ACSF, in mM: 127 NaCl, 25 $NaHCO_3$, 25 D-glucose, 2.5 KCl, 1 $MgCl_2$, 2 $CaCl_2$, and 1.25 NaH_2PO_4, aerated with 95% O_2 / 5% CO_2) at 37°C for 30 min. Slices were subsequently incubated in ACSF at 21–22°C for at least 45–60 min prior to electrophysiological recordings.

2.3 | Whole-cell slice electrophysiology

Electrophysiological recordings from fluorescently labelled CRH-positive (CRH+) neurons in the right CeA of acute brain slices were performed in whole-cell patch-clamp configuration. Briefly, slices were transferred to the recording chamber of a SliceScopePro 6000 (Scientifica, Uckfield, UK) containing an upright microscope (BX51, Olympus, Tokyo, Japan) and PatchStar micromanipulators (Scientifica). Brain slices were held in place with short pieces of flattened gold wire (0.813 mm diameter; Alfa Aesar, Haverhill, MA, USA). CRH+ CeA neurons were identified by red fluorescent protein tdTomato using LED optics (cooled pE-4000). Pipettes for recordings were fabricated from borosilicate capillaries with filaments (G150-F, Warner, Hamden, CT, USA) using a horizontal puller (P-97, Sutter, Novato, CA, USA), and filled with intracellular solution composed of (in mM) 128 potassium gluconate, 10 HEPES, 1 EGTA, 4 $MgCl_2$, 4 ATP and 0.4 GTP, 10 phosphocreatine, 3 ascorbate, and 0.05 Alexa-594 or 488 (Molecular Probes, Eugene, OR, USA); pH 7.3. EGTA was included both to facilitate seal formation and to reduce cytosolic calcium elevations induced by the various stimulus protocols used in these studies. For the neuronal morphological measurement, the biocytin (~4 mg/ml) was added to the intracellular solution. ACSF was used as the extracellular recording solution. Slices were ideally used 1.5–3 h after preparation, but some were used up to 5 h after preparation. Recordings were performed in 10 ml of ACSF (31–33°C) continuously aerated with 95% O_2/5% CO_2 in a re-circulation system driven by a small electric pump. The ACSF in the system was refreshed every 2 h to avoid concentration changes due to evaporation. The recording temperature was controlled by an in-line heating system (TC324B, Warner). Recordings were targeted to neurons 60–100 μm deep in the slice. Intrinsic recordings were performed with synaptic blockers (in μM): 5 CPP (-((R)–2-carboxypi perazin-4-yl)-propyl-1-phosphonic

acid, a selective NMDA receptor antagonist), 10 NBQX (2,3- dioxo-6-nitro-1,2,3,4-tetrahydrobenzo[f]quinoxaline-7-sulfonamide, a selective AMPA receptor antagonist), and 5 GABAzine (4-[6-imino-3-(4-methoxyphenyl)pyridazin-1-yl]butanoic acid hydrobromide, a selective GABA-A receptor antagonist). Pipette capacitance was compensated; series resistance was monitored but not compensated, and required to be <35 MΩ for inclusion in the data set. Current-clamp recordings were bridge-balanced. Current was injected as needed to maintain the membrane potential near −70 mV during select stimulus protocols (i.e., within the activation range of I_h at baseline). Recordings were amplified and filtered at 4 kHz and digitized at 10 kHz using a Multiclamp 700B amplifier (Molecular Devices). Membrane potential values were not corrected for a calculated liquid junction potential of 11 mV (32−33°C). Ephus software was used for data collection. Voltage sag and input resistance were measured from a membrane potential of −70 ± 3 mV. Voltage sag was measured by presenting multiple 1-s hyperpolarizing current steps (−200, −150, −100, and −50 pA). Percentage voltage sag was calculated using the peak voltage (*V*peak) and steady-state voltage (*V*ss) using the equation 100 × (*V*peak − *V*ss)/*V*peak. Input resistance was measured from the steady-state responses to a series of hyperpolarizing and subthreshold depolarizing current steps (duration 1.0 s, amplitude −200 to 100 pA, 50-pA steps), as the slope of a linear least squares fit to the resulting voltage–current relationship. Current threshold for action potentials (APs) was defined as the magnitude of current step that produced at least one AP. Voltage threshold (in mV) for APs was defined as the point when *dV*/*dt* exceeded 10% of its maximum value, relative to a *dV*/*dt* baseline measured 2 ms before the AP peak, which was measured as the maximum membrane potential reached after threshold. AP amplitude was determined by the difference between threshold and peak values. The AP half-width was measured at half-amplitude. The onset of AP firing was measured as the time (in milliseconds) between current step initiation and the threshold of the first AP. Frequency–current relationships were calculated from the numbers of APs per current step, and frequency–current slopes were calculated by linear regression. Spike (or AP) frequency adaptation (SFA) was obtained by acquiring the ratio of the third interspike interval (ISI) to the fifth ISI (fast-SFA) and the ratio of the fifth ISI to the 10th ISI (slow-SFA). Fast and slow SFAs were calculated from responses that produce more than five and 10 APs, respectively.

2.4 | Neuronal morphology and confocal imaging

Slices used for confocal imaging were fixed with 4% paraformaldehyde (PFA) in phosphate buffer solution overnight at 4°C. Following PFA fix (day 1), slices were rinsed in 1× Tris-buffered saline (TBS) for 5 min seven times. Slices were then transferred to 3% TBS-Triton and incubated for 1 h. After this step, the slices were transferred to 10% Normal Goat Serum (NGS) + 0.5% Bovine Serum Albumin (BSA) in TBS for 30 min of incubation. The slices were then rinsed in 1× TBS for 5 min two times. After rinsing, the slices were transferred to the Streptavidin Alexa Fluor 488 conjugate (1:200) in TBS + 1% NGS + 0.5% BSA for ~16 h at 4°C. On day 2, the slices were rinsed in TBS for 5 min four times. Then Dako Fluo mounting medium was used to mount the slices on glass microscope slides. The slices were flanked by cover slip shards (2 × 0.15 mm thick shards) creating a well to prevent smashing the slice. Thin cover glass was placed over the slice and flanking shards, and the edges were sealed with nail polish. Confocal fluorescent images of CRH+ neurons with tdTomato red fluorescent protein were obtained using a Nikon Eclipse Ti inverted microscope equipped with four lasers (405, 488, 561, and 640 nm). A 10× or 20× Plan Apo λ objective was used to scan the slices from top to bottom at 2-μm intervals. Image acquisition was conducted using NIS-Elements (version 5.02) software.

2.5 | Statistical analysis

Custom MATLAB (Mathworks, Natick, MA, USA) routines were used to analyze data off-line. For all data, a Lilliefors test was performed prior to significance testing to determine if the data were normally distributed. Significant differences between multiple independent groups will be determined using a one-way ANOVA for normally distributed data or a Kruskal–Wallis test for nonnormally distributed data. A Bonferroni post hoc analysis was used for multiple comparisons if the one-way ANOVA or Kruskal–Willis test resulted in a significant omnibus *F*-test. Statistical comparisons between two independent groups were performed with the Student's unpaired *t* test (for normally distributed data) or the Wilcoxon rank sum test (for nonnormally distributed data). ImageJ/Fiji software was used to measure soma size and neurite length following previously described methods (Wang et al., 2019). Sholl analyses were conducted on biocytin-filled neurons using a customized Simple Neurite Tracer plugin for Fiji. Error bars in plots represent standard error of the mean (SEM).

2.6 | Chemicals

The chemicals used in this study are as follows: Biocytin (334910, Fisher); Sodium Phosphate Monobasic (RDD007-1KG, Sigma); Sodium Phosphate Dibasic (795410-1KG, Sigma); Tris-Buffered Saline, (TBS, T5030-100TAB, Sigma); Triton X-100 (9002-93-1, Sigma); Normal Goat Serum (NGS, Jackson Immuno Research Laboratories, Inc. Code 005-000-001); Bovine Serum Albumin (BSA, A2153-10G, Sigma); Streptavidin Alexa Fluor 488 conjugate (89-139-566, Fisher); and Paraformaldehyde 16% solution, EM Grade (15710-S, Fisher).

3 | RESULTS

3.1 | Intrinsic and morphological differences between CRH neurons in CeL and CeM

Using the acute brain slices obtained from the CRH-ires-Cre;Ai14 (tdTomato) mice (Figure 1a,b), we observed robust expression of CRH+ neurons in the CeL with weaker expression in the CeM and scarce

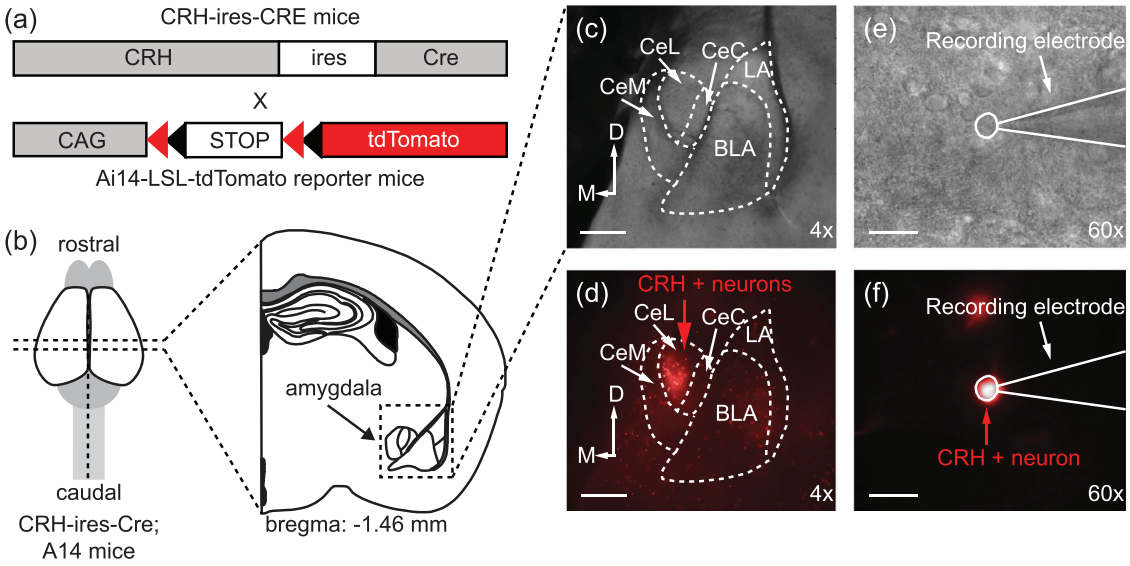

FIGURE 1 Identifying CRH+ CeA neurons for whole-cell recording. (a) CRH-ires-CRE mice were mated with Ai14-LSL-tdTomato reporter mice. (b) Acute coronal brain slices containing the CeA were prepared from CRH-ires-Cre;Ai14 mice. (c) Representative bright-field 4× image of a 300-μm slice containing lateral amygdala (LA), basolateral amygdala (BLA), and the CeA (CeC: laterocapsular; CeL: lateral; CeM: medial). (d) Epifluorescence 4× image showing the expression of CRH+ neurons in the CeA. (e) Representative bright-field 60× image of electrophysiological recording from identified CRH+ CeA neuron from CRH-ires-Cre;Ai14 mice. (f) Epifluorescence 60× image showing electrophysiological recording from identified CRH+ CeA neuron from CRH-ires-Cre;Ai14 mice. D: Dorsal, M: Medial. Scale bar, 330 μm, under 4× magnification. Scale bar, 22 μm, under 60× magnification

expression in the CeC (Figure 1c,d). We also observed moderate expression of CRH neurons in the LA and BLA (Figure 1c,d) as in our previous study (Li & Sheets, 2020). Due to the scant expression of the CRH+ neurons in the CeC, we targeted CRH+ neurons in CeL and CeM for whole-cell electrophysiological recording in acute brain slice (Figures 1e,f and 2a). We recorded 58 CeL-CRH+ neurons and 49 CeM-CRH+ neurons from both male and female mice. Our analysis revealed significant differences in both subthreshold and suprathreshold properties between CeL-CRH+ and CeM-CRH+ neurons. Specifically, CeM-CRH+ neurons were significantly more excitable than CeL-CRH+ in response to increasing step current injections (Figure 2b). In addition, CeM-CRH+ neurons displayed a more depolarized resting membrane potentials, larger voltage sag, larger input resistance, smaller current threshold for AP firing, more hyperpolarized voltage threshold for AP firing, shorter onset to AP firing at threshold, and narrower AP half-widths (Figure 2b–f; Table 1). Next, we asked whether these observed intrinsic differences between CeL-CRH+ and CeM-CRH+ neurons were sex specific. The same analysis of intrinsic properties for CRH+ neurons disaggregated by sex revealed similar intrinsic differences between CeL-CRH+ and CeM-CRH+ neurons (Figure 2g–p; Table 1). However, current threshold, onset to AP firing, and AP half-width were not significantly different between CeL-CRH+ and CeM-CRH+ neurons in male mice (Table 1). These results demonstrated that intrinsic differences between CeL and CeM CRH+ neurons were relatively similar in both male and female mice (Table 1).

Next, we compared the morphology of CRH+ neurons in CeL and CeM (Figure 3a–l; CRH+ CeL neurons n = 10, male n = 5, female n = 5; CRH+ CeM neurons n = 22, male n = 13, female n = 9). Soma area (Figure 3e, CeL = 135.12 ± 12.64; CeM = 167.50 ± 11.14; P = .093, Student's t-test) was greater in CeM-CRH+ than those in CeL-CRH+ neurons, but the difference did not reach statistical significance. Total length of dendrites was not significantly different between CRH+ neurons in CeL and CeM (Figure 3f, CeL = 804.15 ± 75.81 μm; CeM = 910.32 ± 82.85 μm; P = .43, Student's t-test). Additional analysis did reveal other morphological differences between CeL-CRH+ and CeM-CRH+ neurons (Figure 3g–l). Compared to CeL-CRH+ neurons, CeM-CRH+ neurons had significantly greater mean branch length (Figure 3g, CeL = 25.87 ± 2.35 μm; CeM = 50.64 ± 4.93 μm; P = .000097, Student's t-test) including length of longest dendritic branch (Figure 3h, CeL = 102.29 ± 11.59 μm; CeM = 190.06 ± 17.09 μm; P = .00019, Student's t-test). However, CeM-CRH+ neurons displayed significantly fewer number of rendered paths (Figure 3i, CeL = 13.5 ± 1.06; CeM = 9.54 ± 0.61; P = .0018, Student's t-test), branches (Figure 3j, CeL = 33.2 ± 4.12; CeM = 20.09 ± 2.17; P = .0042, Student's t-test), junctions (Figure 3k, CeL = 16.4 ± 2.21; CeM = 9.0 ± 1.17; P = .0029, Student's t-test), and end-points (Figure 3l, CeL = 12.9 ± 0.94; CeM = 9.5 ± 0.57; P = .0030, Student's t-test) compared to CeL-CRH+ neurons.

3.2 | Heterogeneity of intrinsic properties within CeA-CRH+ neurons

We recorded 58 CeL-CRH+ neurons (Figure 4a; 28 neurons from 13 males, 30 neurons from 13 females) and found that the majority (56; 96.6%) displayed a delayed onset of firing at threshold (Figure 4b,e,f).

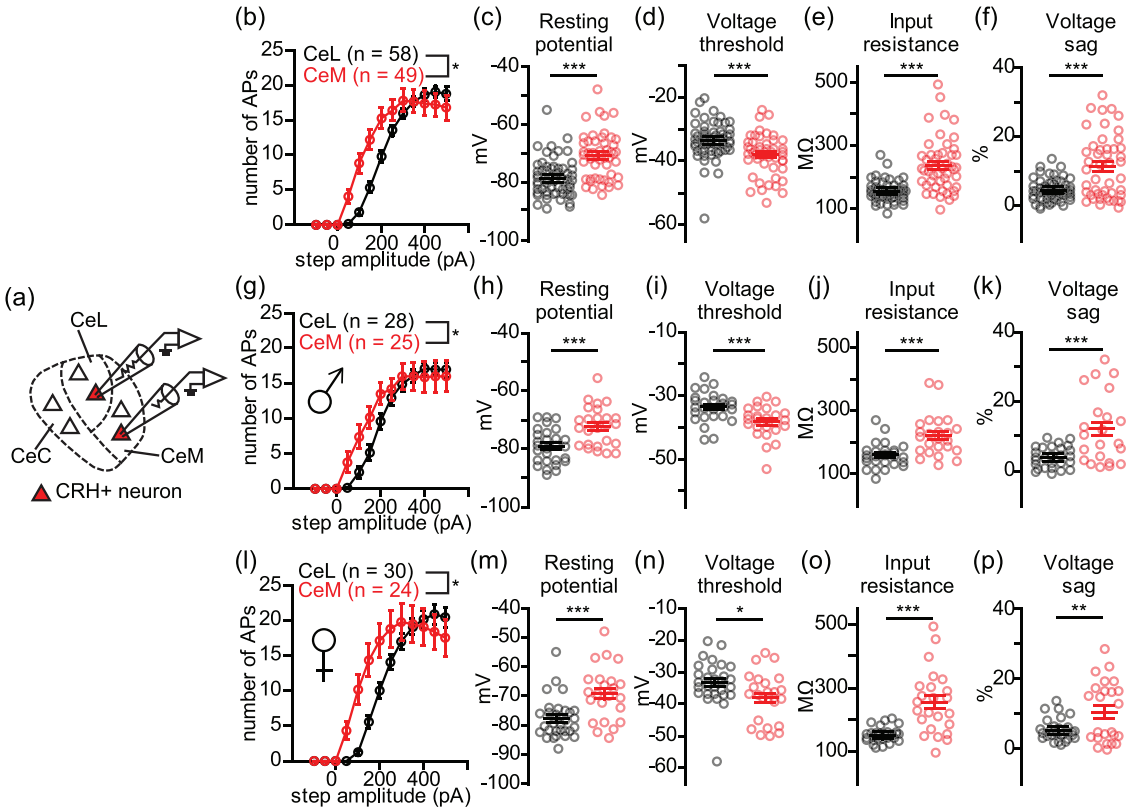

FIGURE 2 CRH+ neurons in the CeL and CeM are intrinsically different. (a) Schematic recording configuration in the CeL and CeM of CRH+ tdTomato mice. (b) Plot of action potential (AP) number versus current injection values showing higher excitability in CeM-CRH+ neurons than that in CeL-CRH+ neurons from mice of both sexes. (c–f) Scatter plots with mean ± SEM to display comparisons of resting potential, voltage threshold, input resistance, and voltage sag between CeL and CeM CRH+ neurons from mice of both sexes. (g) Plot of AP number versus current injection values showing higher excitability in CeM CRH+ neurons than that in CeL-CRH+ neurons from male mice. (h–k) Scatter plots with mean ± SEM to display comparisons of resting potential, voltage threshold, input resistance, and voltage sag between CeL and CeM CRH+ neurons from male mice. (l) Plot of AP number versus current injection values showing higher excitability in CeM CRH+ neurons than that in CeL CRH+ neurons from female mice. (m–p) Scatter plot with mean ± SEM to display comparisons of resting potential, voltage threshold, input resistance, and voltage sag between CeL and CeM CRH+ neurons from female mice. $^{*}P < .05$; $^{**}P < .01$; $^{***}P < .001$

This firing property has been denoted previously as a "late-firing" phenotype (Hunt et al., 2017; Li et al., 2013; Li & Sheets, 2018). Two CeL-CRH+ neurons recorded displayed a bursting and regular-firing phenotype (Figure 4c–f), which are also described in previous studies (Dumont et al., 2002; Kiritoshi & Neugebauer, 2018; Li & Sheets, 2018). In contrast to CeL-CRH+ neurons, CeM-CRH+ neurons displayed intrinsic heterogeneity. In CeM-CRH+ neurons (25 neurons from nine males, 23 neurons from nine females), 14 (29.2%) displayed late-firing, 14 (29.2%) displayed regular-firing, 12 (25.0%) displayed bursting, and eight (16.7%) were fast-spiking (Figure 5a–g). We did not detect any significant differences in intrinsic properties between CRH+ late-firing neurons recorded from CeL and CeM (Table 2). However, our analysis showed significant differences in both subthreshold and firing properties between different phenotypes of CeM-CRH+ neurons (Figure 5g–l; Table 2). We did not perform the electrophysiological recordings in the CeC due to the scarce expression of CRH+ neurons. Overall, these results demonstrated that CRH+ neurons display unique intrinsic profiles depending on topographical location within adjacent subregions (i.e., CeM and CeL) of the CeA.

Previous work has also reported rostrocaudal differences in both topographical distribution and intrinsic properties of specific CeA neuronal subclasses including CRH-CeA neurons (Adke et al., 2021; Hartley et al., 2019; Sanford et al., 2017). We observed that CRH-CeA neurons were distributed mainly in the CeL and CeM from caudal (−1.70 and −1.58 mm to bregma) and middle (−1.46 and −1.22 mm to bregma) sections of CeA with sparser expression in more rostral CeA sections (Figure 6a–d). Therefore, our recordings were focused mainly on caudal and middle sections of CeA (Figure 7a). We analyzed whether AP threshold, AP frequency–current slope, and AP half-width correlated with rostrocaudal location of the intrinsically distinct subtypes of CRH-CeA neurons (Figure 7b–d). We found a significant positive correlation for the slope of AP frequency over injected step current in CeL-CRH+ late-firing neurons with neurons in more caudal CeL showing higher firing rates in response to increasing injected current (Figure 7c). Both AP threshold and AP half-width were not correlated with rostrocaudal location (Figure 7b,d). In the CeM, only AP threshold in fast-firing CRH+ neurons was significantly negatively correlated with rostrocaudal location with more caudal neurons showing a lower

TABLE 1 Comparison of intrinsic properties between CeL and CeM CRH+ neurons

	Total		Male		Female	
Neuronal population CRH+ CeA neurons	**CeL ($n = 58$) $n = 26$ animals**	**CeM ($n = 49$) $n = 18$ animals**	**CeL ($n = 28$) $n = 13$ animals**	**CeM ($n = 25$) $n = 9$ animals**	**CeL ($n = 30$) $n = 13$ animals**	**CeM ($n = 24$) $n = 9$ animals**
Subthreshold properties						
Resting potential (mV)	−78.5 ± 0.84	−70.8 ± 1.15***	−79.19 ± 1.12	−72.31 ± 1.36***	−77.79 ± 1.26	−69.32 ± 1.85***
Voltage sag (%)	4.63 ± 0.42	11.31 ± 1.31***	4.02 ± 0.57	12.13 ± 1.94***	5.22 ± 0.59	10.49 ± 1.78**
Input resistance (MΩ)	156.44 ± 4.23	237.51 ± 12.24**	160.11 ± 7.34	220.88 ± 13.34**	152.90 ± 4.38	254.14 ± 20.26***
Firing properties						
I threshold (pA)	108.77 ± 5.33	90.82 ± 4.98*	105.36 ± 8.66	94 ± 6.00	112.07 ± 6.40	87.5 ± 8.10*
V threshold (mV)	−33.5 ± 0.76	−38.2 ± 0.92***	−33.69 ± 0.87	−38.36 ± 1.01****	−33.32 ± 1.24	−38.06 ± 1.59*
Onset (ms)	0.19 ± 0.011	0.10 ± 0.014**	0.19 ± 0.018	0.14 ± 0.022	0.19 ± 0.014	0.069 ± 0.014***
Frequency/current (Hz/pA)	0.17 ± 0.0066	0.25 ± 0.023***	0.17 ± 0.0096	0.23 ± 0.028*	0.18 ± 0.0091	0.27 ± 0.037*
Half-width (ms)	0.80 ± 0.034	0.67 ± 0.044*	0.84 ± 0.044	0.80 ± 0.071	0.77 ± 0.053	0.54 ± 0.033***
Height (mV)	66.57 ± 1.5	64.1 ± 1.69	67.22 ± 1.89	65.27 ± 2.51	65.95 ± 2.34	62.89 ± 2.28
Spike frequency adaptation ($3^{rd}/5^{th}$)	1.09 ± 0.079	3.3 ± 2.4	1.03 ± 0.041	0.96 ± 0.097	1.15 ± 0.15	5.82 ± 5.01
Fast afterhyperpolarization (mV)	−7.14 ± 0.93	−5.36 ± 0.90	−6.0 ± 0.62	−4.73 ± 0.95	−8.20 ± 1.68	−6.01 ± 1.55

Note: Data are shown as mean ± SEM. Student's *t*-test;
*$P < .05$;
**$P < .01$;
***$P < .001$.

TABLE 2 Comparison of intrinsic properties for CeL and CeM CRH+ neurons with distinct firing patterns

CRH+ CeA neurons	**CeL late-firing neurons ($n = 56$) $n = 26$ animals**	**CeM late-firing neurons ($n = 14$) $n = 8$ animals**	**CeM regular-firing neurons ($n = 14$) $n = 11$ animals**	**CeM burst-firing neurons ($n = 12$) $n = 12$ animals**	**CeM fast-spiking neurons ($n = 8$) $n = 8$ animals**	**Significance**
Subthreshold properties						
Resting potential (mV)	−78.4 ± 0.9	−77.2 ± 1.7	−68.9 ± 1.6	−70.7 ± 1.8	−63.2 ± 3.2	b, c, d, e, g***^
Voltage sag (%)	4.6 ± 0.4	6.7 ± 1.1	9.8 ± 2.9	18.0 ± 2.9	12.7 ± 2.3	c, d***^
Input resistance (MΩ)	156.7 ± 4.4	164.0 ± 8.0	280.7 ± 26.2	257.3 ± 16.3	268.5 ± 35.8	b, c, d, e, f, ***^
Firing properties						
I threshold (pA)	110 ± 5.4	110.7 ± 5.7	85.7 ± 9.7	66.7 ± 7.1	93.8 ± 14.8	c, f***^
V threshold (mV)	−33.2 ± 0.8	−35.2 ± 0.8	−43.3 ± 1.5	−39.2 ± 2.0	−33.8 ± 2.2	b, c, e, i***#
Onset (ms)	0.19 ± 0.01	0.24 ± 0.02	0.03 ± 0.003	0.07 ± 0.01	0.05 ± 0.008	b, c, d, e, f, g***^
Frequency/current (Hz/pA)	0.17 ± 0.01	0.18 ± 0.01	0.28 ± 0.06	0.18 ± 0.04	0.4 ± 0.03	b, d, g, i, j***#
Half-width (ms)	0.81 ± 0.04	1.02 ± 0.09	0.54 ± 0.03	0.63 ± 0.04	0.40 ± 0.02	b, d, e, f, g***^
Height (mV)	66.32 ± 1.5	73.66 ± 1.6	59.7 ± 3.4	63.2 ± 3.0	57.8 ± 4.2	e, g**#
Spike frequency adaptation ($3^{rd}/5^{th}$)	1.09 ± 0.08	0.98 ± 0.04	1.06 ± 0.14	10.6 ± 10.04	0.91 ± 0.12	c**^
Fast afterhyperpolarization (mV)	−7.4 ± 0.94	−7.3 ± 0.93	−3.4 ± 1.2	−2.9 ± 2.8	−8.2 ± 1.6	None^

Note: Data are shown as mean ± SEM. a, CeM late-firing versus CeL late-firing; b, CeM regular-firing versus CeL late-firing; c, CeM burst-firing versus CeL late-firing; d, CeM fast-spiking versus CeL late-firing; e, CeM regular-firing versus CeM late-firing; f, CeM burst-firing versus CeM late-firing; g, CeM fast-spiking versus CeM late-firing; h, CeM burst-firing versus CeM regular-firing; i, CeM fast-spiking versus CeM regular-firing; j, CeM fast-spiking versus CeM burst-firing. #ANOVA (normally distributed data) or ^Kruskal–Wallace test (nonnormally distributed data) followed by a Bonferroni post hoc analysis for multiple comparisons was used to determine statistical significance.
*$P < .05$;
**$P < .01$;
***$P < .001$

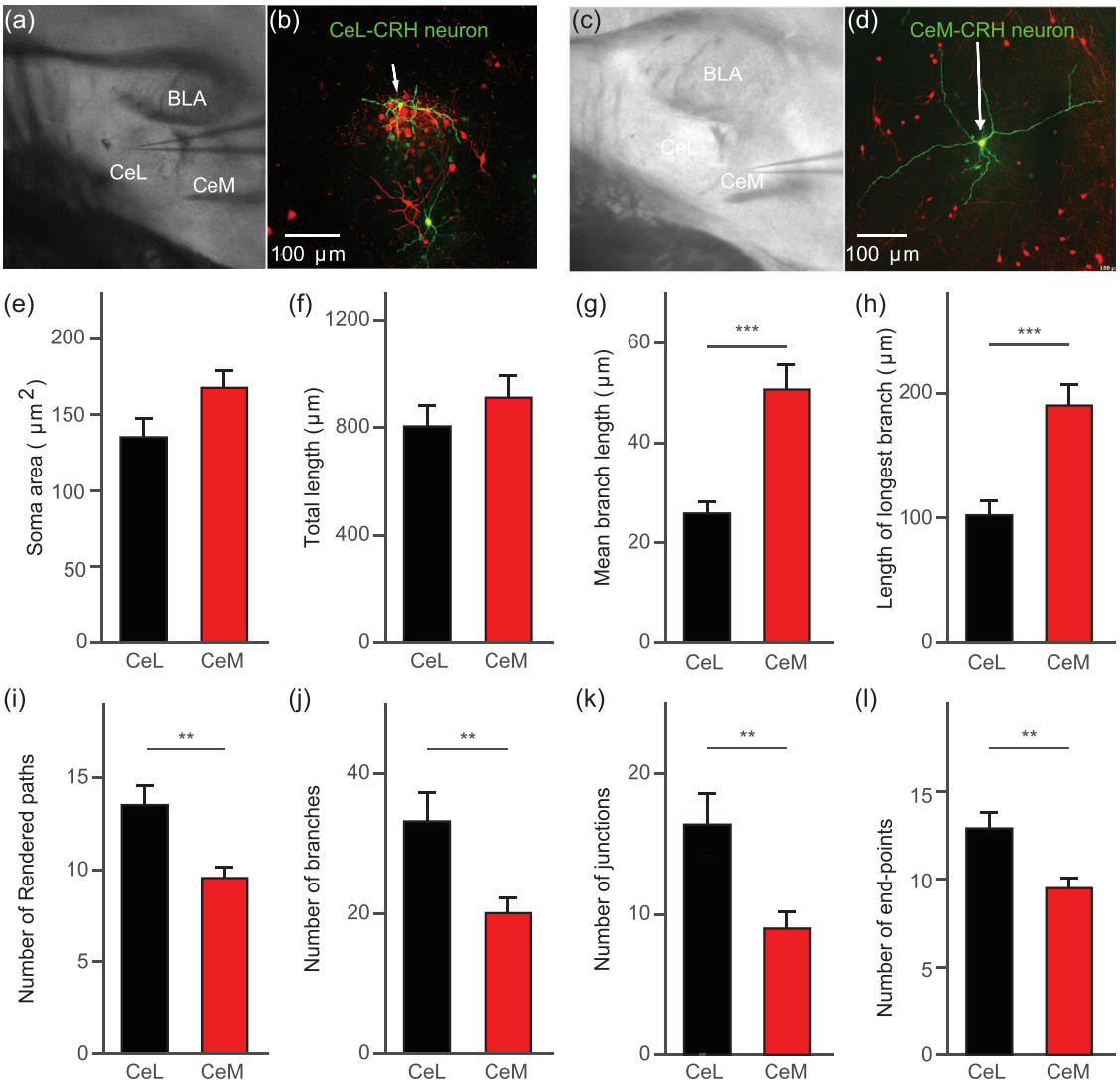

FIGURE 3 Morphological difference of CRH+ neurons between the CeL and CeM. (a) Bright field image of recording configuration in the CeL. (b) Confocal image showing imaged CeL-CRH+ neurons (green) recorded in acute brain slice of CRH-tdTomato mice. (c) Bright-field image of recording configuration in the CeM. (d) Confocal image showing imaged CeM-CRH+ neurons (green) recorded in acute brain slice of CRH-tdTomato mice. (e–l). Bar plots with mean ± SEM to display comparisons of soma area, total dendrite length, mean dendrite branch length, length of longest dendritic branch, number of rendered paths, number of branches, number of junctions, and number of end points between imaged CeL and CeM CRH+ neurons. Student's *t*-test; $^{**}P < .01$; $^{***}P < .001$

threshold for AP firing (Figure 7e). Both AP half-width and slope of AP frequency/current were not correlated with rostrocaudal location for any subclasses of CeM-CRH+ neurons (Figure 7f–g).

3.3 | Firing phenotype correlates with the morphology of CeA-CRH neurons

Our next goal was to dissect the morphology between intrinsically distinct CRH neurons in the CeL and CeM (Figure 8). For this, we first identified the intrinsic profile for CeL-CRH+ or CeM-CRH+ neurons using slice electrophysiology and subsequently imaged the recorded neurons by staining for biocytin (see Section 2), which was included in the intracellular recording solution (Figure 8). Morphological analysis revealed that CeL ($n = 9$ neurons; male = 5, female = 4) and CeM ($n = 6$ neurons; male = 5, female = 1) CRH+ late-firing neurons displayed similar morphological properties (Figures 8a–j, 9a–d, and 10; Table 3). Dendrites of CeL-CRH+ late-firing neurons were contained within the CeL boundary (Figure 10a). Dendrites of CeM-CRH+ late-firing neurons also stayed within the CeM boundary (Figure 10b). Sholl analyses did not show significant differences in the number of intersections between CeL-CRH+ and CeM-CRH+ late-firing neurons demonstrating similar dendritic complexity (Figure 9e). A majority of late-firing neurons (12 of total 15 neurons; Figure 10a–b) in CeL and CeM closely resembled the medium-size spiny neurons in the rat CeA (Amano et al., 2012; Cassell & Gray, 1989; Cassell et al., 1999; Chieng et al., 2006; Martina et al., 1999; McDonald, 1982; Schiess et al., 1999; Sun & Cassell, 1993). These 12 late-firing neurons displayed three to

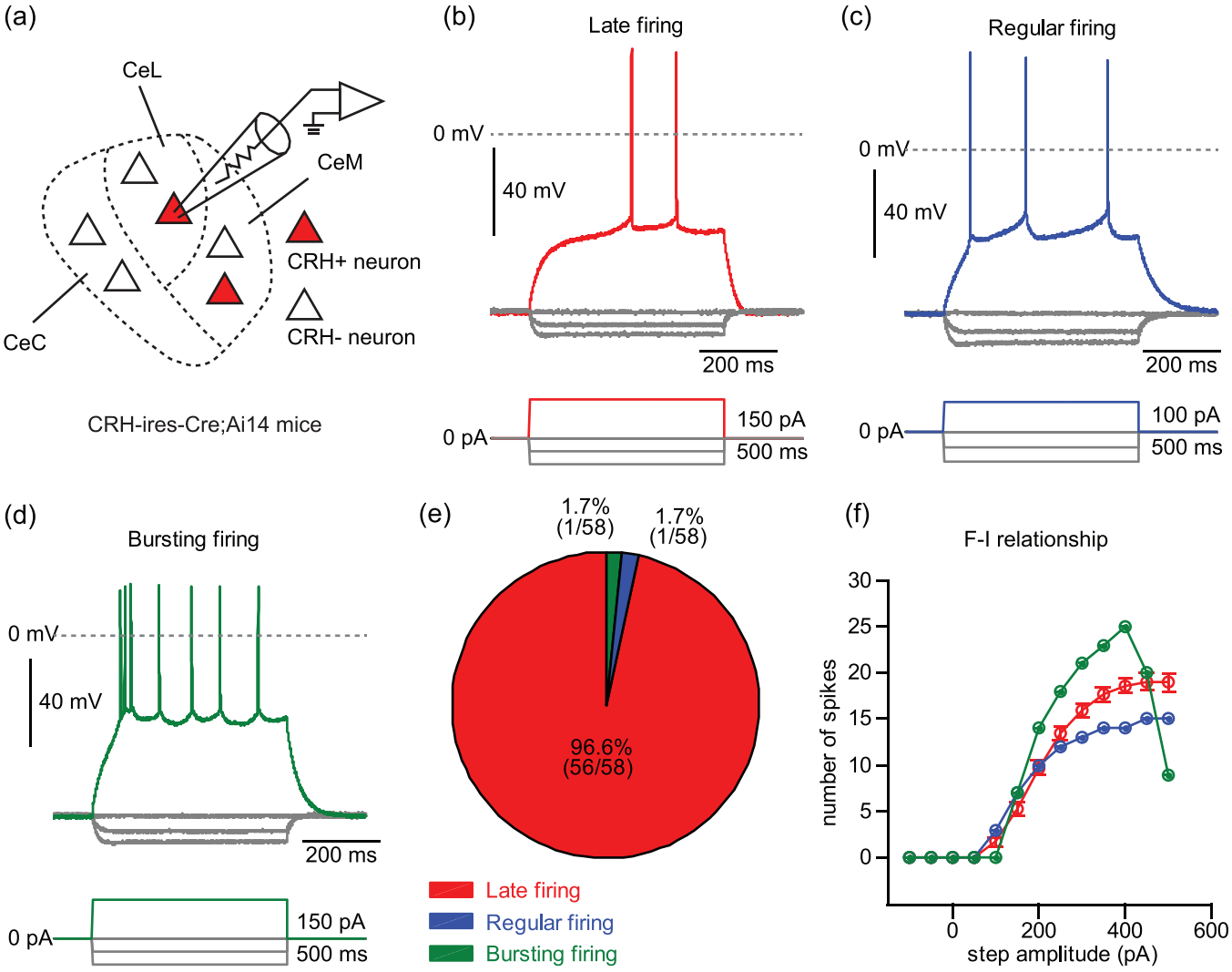

FIGURE 4 The intrinsic homogeneity of CeL CRH+ neurons. (a) Schematic recording configuration in the CeL of CRH+ tdTomato mice. Example traces of (b) late-firing, (c) regular-firing, and (d) bursting CeL-CRH+ neurons. (e) Proportion of distinct CeL-CRH+ subtypes identified by whole-cell electrophysiological recordings. (f) Plot of APs versus current injection values for the three intrinsically distinct CeL-CRH+ subtypes

eight primary dendrites radiating in all directions to form a spherical dendritic field with primary and distal branches displaying a tufted morphology (Figures 10a1–a8 and 10b1–b4). Three of the total 15 late-firing neurons (1 CeL, 2 CeM; Figures 10a9 and 10b5,b6) were smaller with two primary dendrites emerging from opposite poles of the cell body resembling the bipolar (fusiform neurons described in a previous study; Cassell & Gray, 1989). In summary, these results suggest that the morphology of CRH+ late-firing neurons is primarily homogeneous independent of CeA subregion, but a small subset of these neurons display a unique bipolar morphology.

We found that CeM-CRH+ neurons displayed considerable heterogeneity in morphology (Figures 8k–y and 11). Morphological profiles of regular firing CeM-CRH+ neurons ($n = 6$; 3 male, 3 female) revealed multipolar neurons with three to four primary dendrites (Figure 11a). Some of these regular firing neurons possessed long primary projecting dendrites ($n = 4$, 2 male, 2 female; Figure 11a1–a4) that resembled pyriform-like or fusiform-like neurons (Figure 8n,o). Two neurons possessed only one long primary projecting dendrite with several very short primary dendrites (1 male, 1 female; Figure 11a5,a6). All CeM-CRH+ regular firing neurons displayed fewer secondary and more distal dendritic branches compared to late-firing CRH+ neurons. However, the length of longest branch and mean branch length for CeM-CRH+ regular firing neurons was significantly longer than the CeL-CRH and CeM-CRH late-firing neurons (Table 3). A majority (7/8) of bursting CeM-CRH+ neurons displayed dendrites reaching into the CeL (Figure 11b1–b7). This property resembled previously described G2 neurons showing at least one dendrite passing into the CeL (Cassell & Gray, 1989). The typical shape of bursting CeM-CRH+ neurons (4/8) resembled the letter "y" with one long primary dendrite extending to the CeL (Figures 8t and 11b1–b4) and resembled the shape of bursting CeL neurons described in male Sprague–Dawley rats (Amano et al., 2012). A subset of bursting CeM-CRH+ neurons (3/8) were irregular with dendrites branching into the CeL (Figure 11b5–b7). The remaining bursting CeM-CRH+ neuron (1/8) was a bipolar neuron

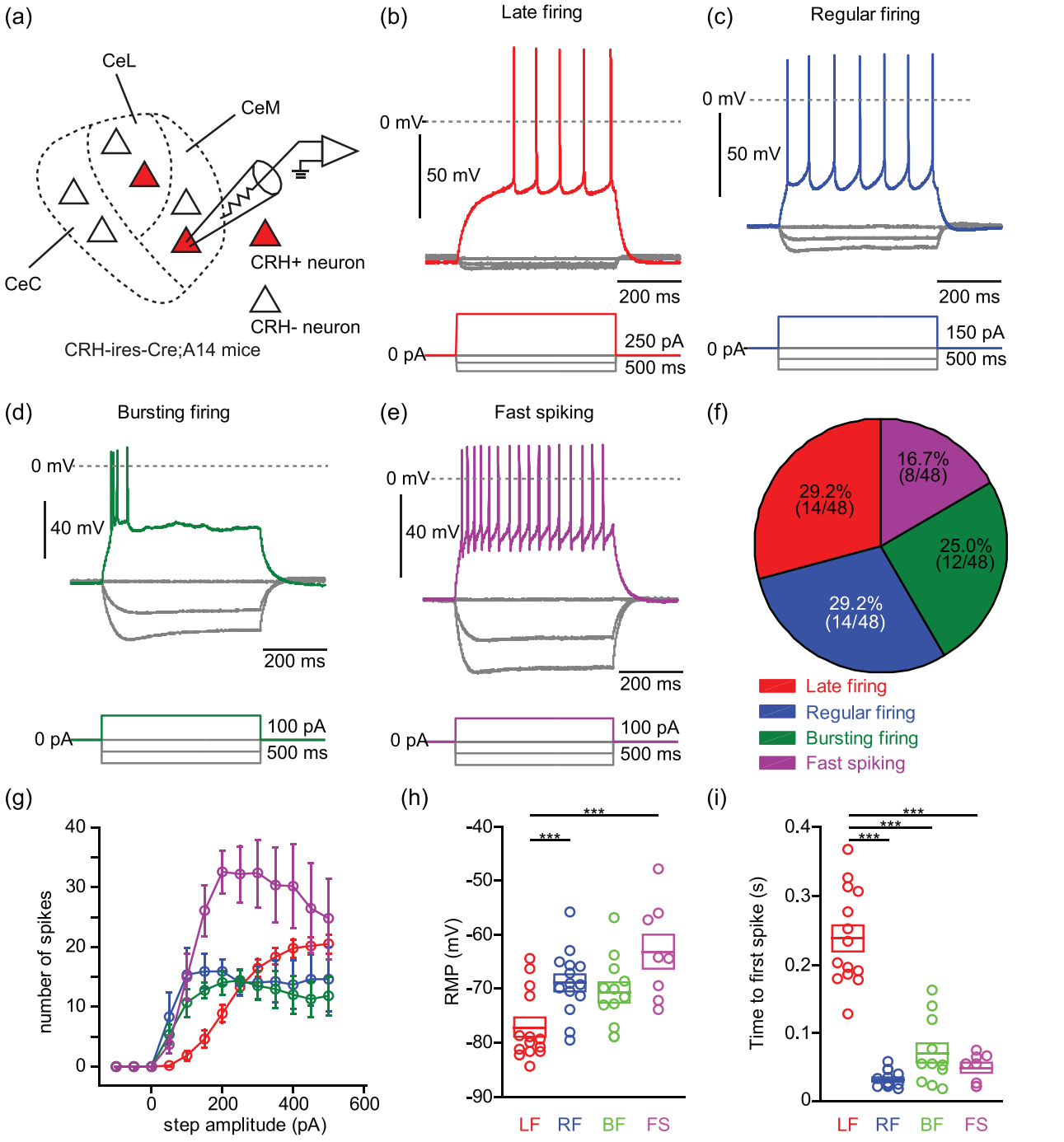

FIGURE 5 The intrinsic heterogeneity of CeM-CRH+ neurons. (a) Schematic recording configuration in the CeM of CRH+ tdTomato mice. Example traces of (b) late-firing, (c) regular-firing, (d) bursting, and (e) fast-spiking CeM CRH+ neurons. (f) Proportion of distinct CeM CRH+ subtypes identified by whole-cell electrophysiological recordings. (g) Plot of AP number versus current injection values in four intrinsically distinct CeM CRH+ subtypes. (h and i) Boxplots displaying comparisons of resting potential and onset time to first AP at firing threshold. Kruskal–Wallis test; $^{***}P < .001$

with one branch extending to the BLA and leaving the other branch in the CeM (Figure 11b8). In general, all bursting CRH+ neurons in our studies showed fewer primary dendrites (three to four dendrites) in addition to fewer secondary and more distal dendritic branches; therefore, the appearance of dendritic trees looked quite simple compared to other phenotypes. Based on the small number of electrophysiologically identified fast-spiking CeM-CRH neurons, we only obtained three successfully filled neurons to perform morphological experiments (Figures 8u–y and 11c). Interestingly, CeM-CRH fast-spiking neurons expressed primary dendrites oriented tangential to the border of the CeL but not extending into the CeL (Figure 11c). The incidence of neurons with dendrites reaching CeL was significantly

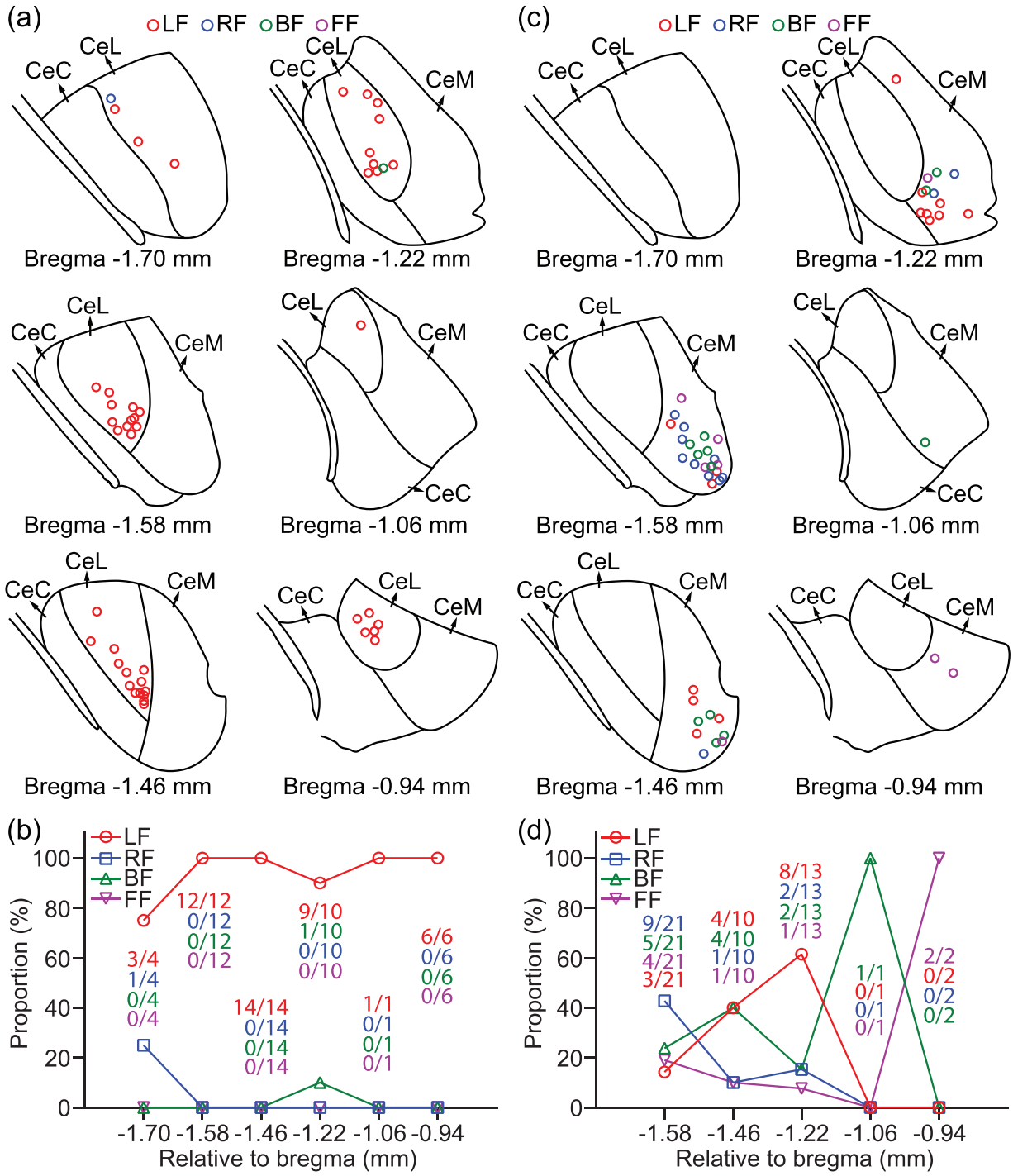

FIGURE 6 Anatomical location of CRH+ neurons recorded in the CeA. (a) Rostrocaudal anatomic locations of recorded CRH+ neurons in the CeL. (b) Number and proportion of intrinsically defined CRH+ neurons recorded along the rostrocaudal axis in the CeL. (c) Rostrocaudal anatomic locations of recorded CRH+ neurons in the CeM. (d) Number and proportion of intrinsically defined CRH+ neurons recorded along the rostrocaudal axis in the CeM

higher in bursting CeM-CRH neurons (7/8) than regular-firing (1/6) and fast-spiking (0/3) CeM-CRH neurons ($P < .05$, Fisher exact test). Whether the property of the preferred orientation of the dendrites in bursting CeM-CRH neurons exists in other bursting CeA neurons with distinct molecular markers needs to be detected in future studies.

There was no significant difference for the soma area, number of rendered paths, number of branches, number of end-points, and arbor area between the different intrinsic groups of CeL and CeM CRH+ neurons (Figure 9a; Table 3). Similar to CeM-CRH+ regular firing neurons, length of longest branch for CeM-CRH+ bursting neurons was significantly longer than late-firing CRH+ neurons in CeL and CeM, but

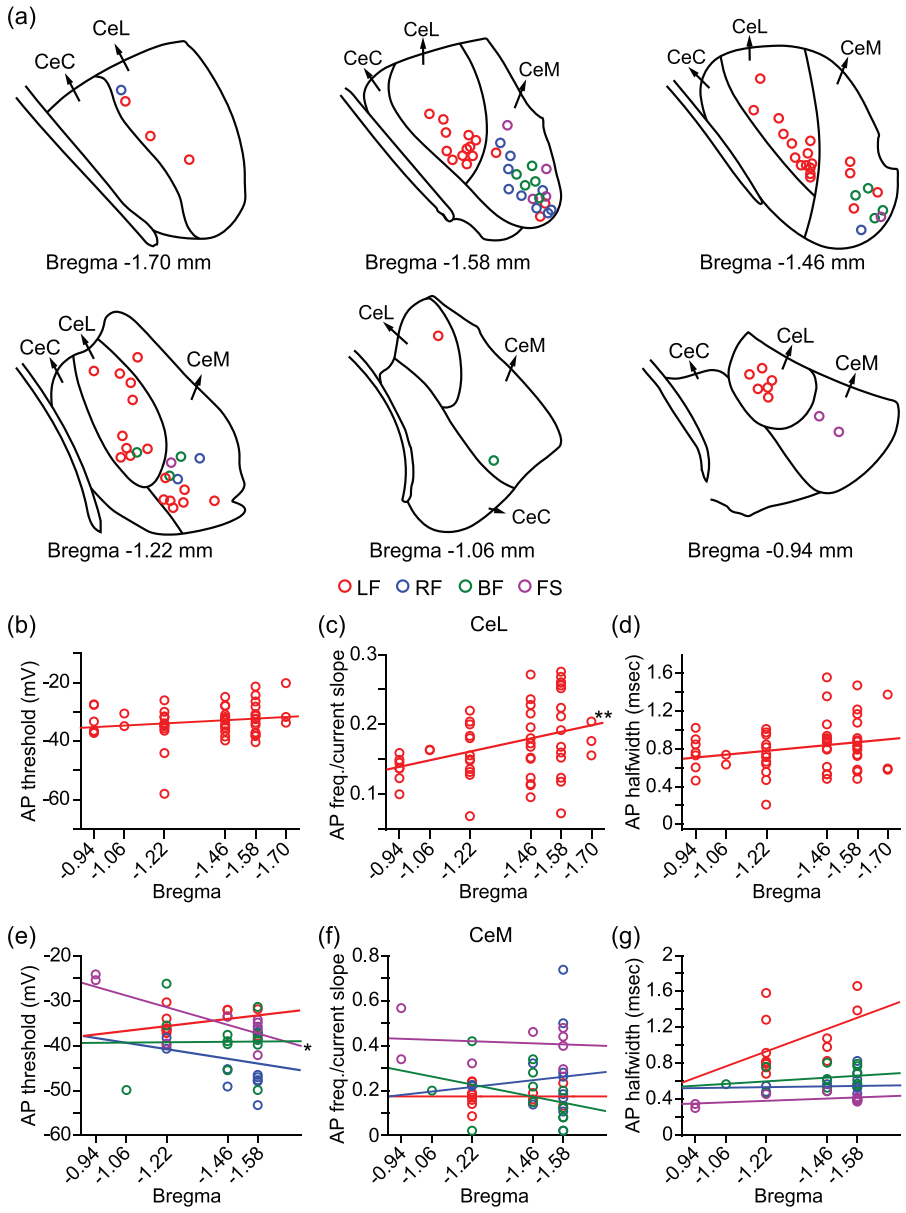

FIGURE 7 Correlation of intrinsic properties with rostrocaudal location of the different subtypes of CeA-CRH+ neurons. (a) Representative schematics of recording locations for late-firing (LF), regular-firing (RF), bursting (BF), and fast-spiking (FS) CeA-CRH+ neurons. Linear regression analysis for (b) AP threshold ($R^2 = .04$, $P = .18$), (c) AP frequency–current slope ($R^2 = .13$; $^{**}P = .01$), and (d) AP half-width ($R^2 = .05$; $P = .11$) for CeL-CRH+ LF neurons

mean branch length of CeM-CRH+ bursting neurons was significantly longer only compared to CeL-CRH+ late-firing neurons (Figure 9b,c; Table 3). However, arbor area did not significantly differ between groups (Figure 9d; Table 3). Lastly, Sholl analysis revealed the distinct complexity of dendritic trees in the intrinsically defined CRH+ CeA neurons within distinct subregions (Figure 9e).

4 | DISCUSSION

Our goal for this study was to dissect the potential intrinsic and morphological heterogeneity of CRH-expressing neurons in topographically distinct substructures of the CeA in mice. The summarized main findings are as follows: (1) the intrinsic and morphological properties between CRH+ neurons in CeL and CeM subregions of the CeA were significantly different in both male and female mice; (2) CRH+ neurons in the CeL consist of relatively homogeneous intrinsic and morphological phenotypes, but CRH+ neurons in the CeM are highly heterogeneous phenotypes in intrinsic and morphological properties in mice of both genders; and (3) the distinct firing phenotypes of CeA neurons were associated with specific morphological properties.

Here, we report CeL-CRH neurons consist of an intrinsically homogeneous phenotype (96.6% late-firing), but CeM-CRH neurons are intrinsically heterogeneous (29.2% late-firing, 29.2% regular firing,

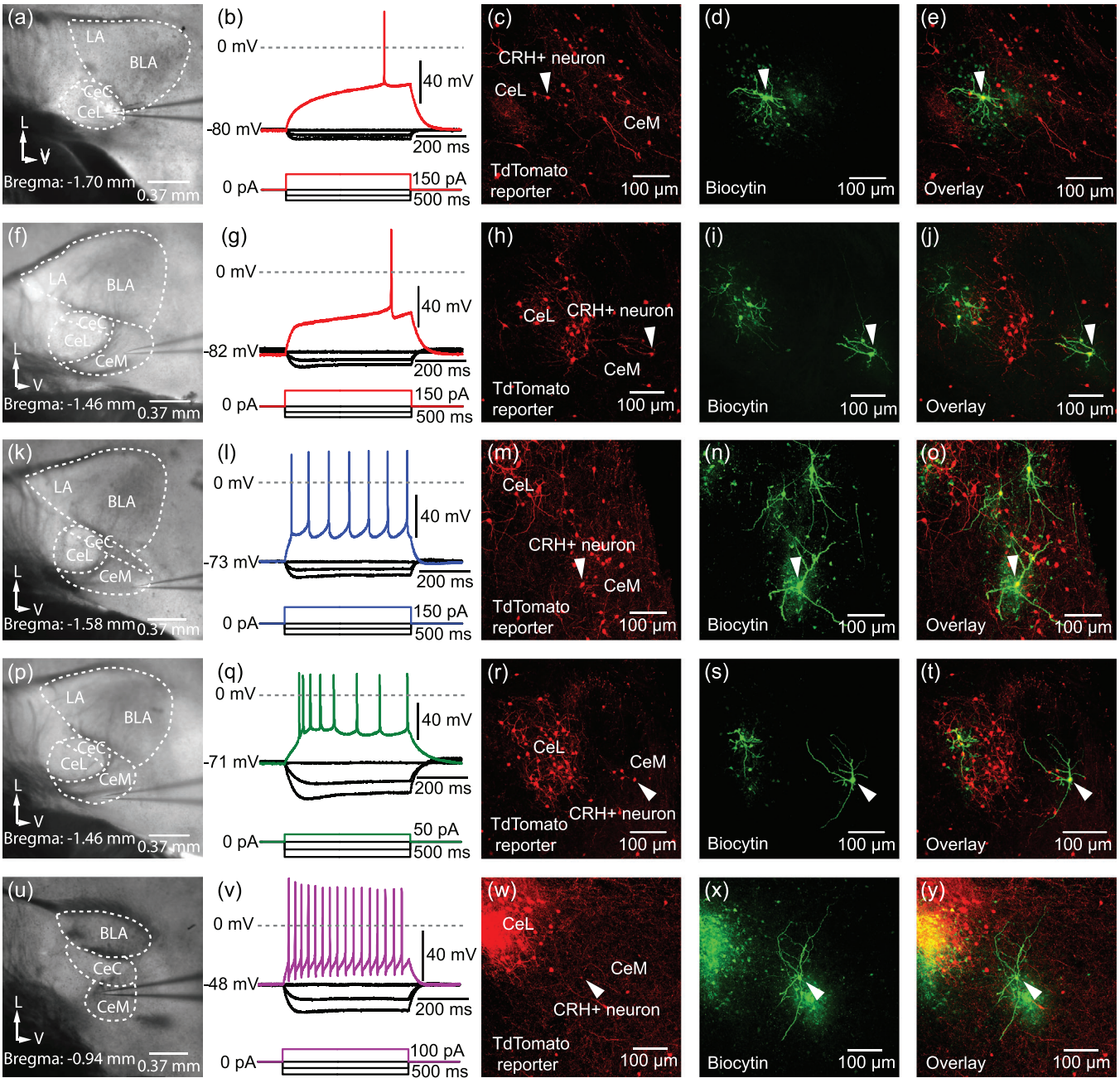

FIGURE 8 Topography, morphology, and intrinsic excitability across CeA-CRH+ neurons. (a) Representative bright-field image of electrophysiological recording from an identified CeL-CRH+ neuron from CRH-ires-Cre;Ai14 mice. (b) A representative action potential of a late-firing CeL-CRH+ neuron. (c) Confocal image (20× magnification) showing the CRH+ neuron recorded with tdTomato reporter. (d) Confocal image (20× magnification) showing the morphology of single CeL-CRH+ neuron recorded with tdTomato reporter filled with biocytin during whole-cell patch clamp recordings. (e) Confocal image (20× magnification) showing the overlay between tdTomato and biocytin in the CeL-CRH late-firing neuron. (f–y) Bright-field recording images, action potential traces, tdTomato labeling, biocytin imaging, and overlay for (f–j) a late-firing CeM-CRH+ neuron, (k–o) a regular-firing CeM-CRH neuron, (p–t) a bursting CeM-CRH neuron, and (u–y) a CeM-CRH+ fast-spiking neuron. L: lateral, V: ventral

25.0% bursting, 16.7% fast-spiking phenotypes). Similarly, the morphology of the CRH+ neurons mainly showed homogeneity in the CeL and heterogeneity in the CeM. These results are similar to findings that show a majority of neurons expressing protein kinase C- δ (PKC-δ+) in the CeL display a late-firing phenotype with a smaller subset showing regular firing (Haubensak et al., 2010). However, another study reported an equal prevalence of late-firing unaccommodating and early-spiking accommodating phenotypes in PKC-δ+ CeL neurons recorded in mice (Hunt et al., 2017). Recordings from somatostatin-expressing (SOM+) CeL neurons in mice have revealed both regular firing and late-firing phenotypes (Li et al., 2013; Mork et al., 2022). It has been reported that approximately 50% of CeL-SOM+ neurons

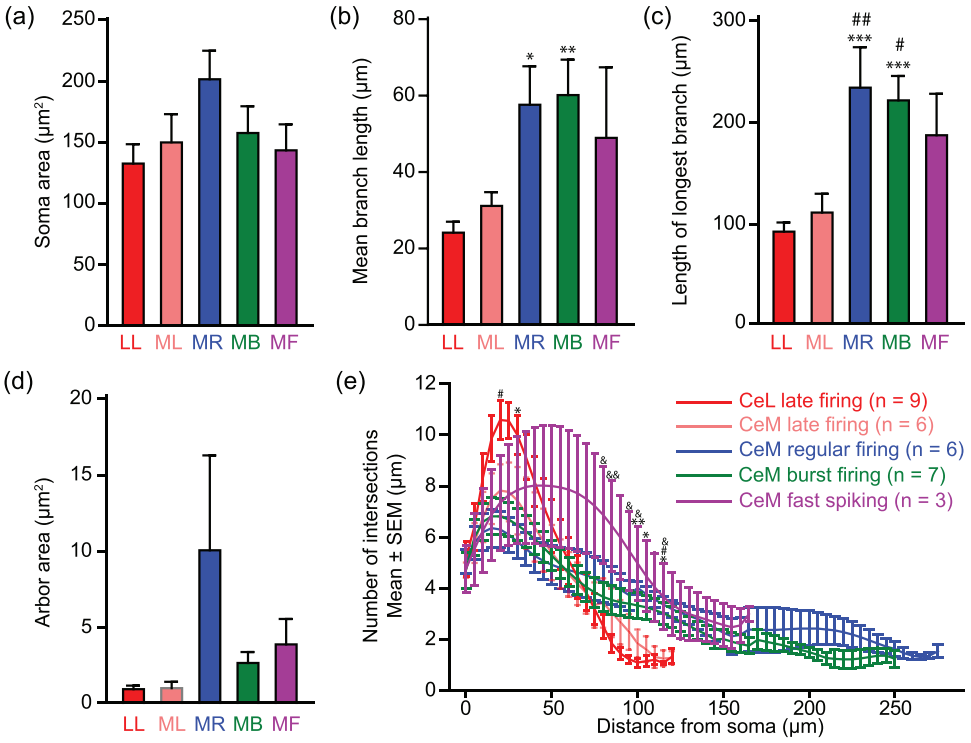

FIGURE 9 The morphological differences of distinct firing CRH+ subtypes in CeL and CeM. (a–d) Column chart displaying comparisons of soma area, mean branch length, length of longest branch, and arbor area between CeL late-firing (LL), CeM late-firing (ML), CeM regular-firing (MR), CeM bursting (MB), and CeM fast-spiking (MF) CRH+ neurons. MR versus LL: $^{*}P < .05$; MB versus LL: $^{**}P < .01$; MR versus LL and MB versus LL: $^{***}P < .001$; MB versus ML: $^{\#}P < .05$; MR versus ML: $^{\#\#}P < .01$. (e) Dendrite Sholl analysis showed the difference of number of intersections between CeL late-firing, CeM late-firing, CeM regular-firing, CeM bursting, and CeM fast-spiking CRH+ neurons. CeL late versus CeM regular: $^{*}P < .05$; CeL late versus CeM regular: $^{**}P < .01$; CeL late versus CeM burst: $^{\#}P < .05$; CeL late versus CeM fast: $^{\&}P < .05$; CeL late versus CeM fast: $^{\&\&}P < .01$

TABLE 3 Morphological parameters of intrinsically distinct CeL and CeM CRH+ neurons

Firing type	CeL late ($n = 9$)	CeM late ($n = 6$)	CeM regular ($n = 6$)	CeM burst ($n = 7$)	CeM fast ($n = 3$)
Parameter					
Soma area (μm^2)	134.4 ± 14.1	151.9 ± 21.1	203.5 ± 21.5	159.6 ± 20.0	145.3 ± 19.4
Rendered paths (#)	13.4 ± 1.2	9.5 ± 1.1	8.8 ± 0.9	9.0 ± 0.92	12.3 ± 3.0
Total length (μm)	753.0 ± 62.6	648.3 ± 113.6	988.6 ± 170.5	892.3 ± 77.58	1319.8 ± 342.9&
Mean branch length (μm)	24.7 ± 2.3	31.8 ± 3.0	58.2 ± 9.5*	60.8 ± 8.7**	49.6 ± 17.9
Length of longest branch (μm)	92.38 ± 6.71	111.06 ± 16.37	233.9 ± 37.6$^{***\#\#}$	221.4 ± 21.7$^{***\#}$	187.2 ± 38.5
Branches (#)	33 ± 4.6	20.7 ± 3.2	17.83 ± 3.05	17 ± 3.7	30.7 ± 9.9
Junctions (#)	16.2 ± 2.5	9.5 ± 1.7	7.7 ± 1.4	7.3 ± 2.1*	14.7 ± 5.4
End-points (#)	12.8 ± 1.0	9.5 ± 1.0	9.0 ± 1.0	8.9 ± 0.8	12 ± 2.6
Arbor area ($\times 10^3\ \mu m^2$)	10.5 ± 0.9	11.2 ± 2.8	101.6 ± 60.7	27.8 ± 5.6	39.9 ± 15.3

Note: Total length: CeM fast versus CeM late, $\&P = .0371$, one-way ANOVA, passed normality test.
Mean branch length: CeM regular versus CeL late,
$^{*}P = .0123$, one-way ANOVA, passed normality test. Mean branch length: CeM burst versus CeL late,
$^{**}P = .0041$, one-way ANOVA, passed normality test. Length of longest branch: CeM regular versus CeL late,
$^{***}P = .0005$, one-way ANOVA, passed normality test. Length of longest branch: CeM burst versus CeL late,
$^{***}P = .0010$, one-way ANOVA, passed normality test. Length of longest branch: CeM regular versus CeM late,
$^{\#\#}P = .0067$, one-way ANOVA, passed normality test. Length of longest branch: CeM burst versus CeM late,
$^{\#}P = .0126$, one-way ANOVA, passed normality test. Junctions: CeM burst versus CeL late, $^{*}P = .0290$, one-way ANOVA, passed normality test.

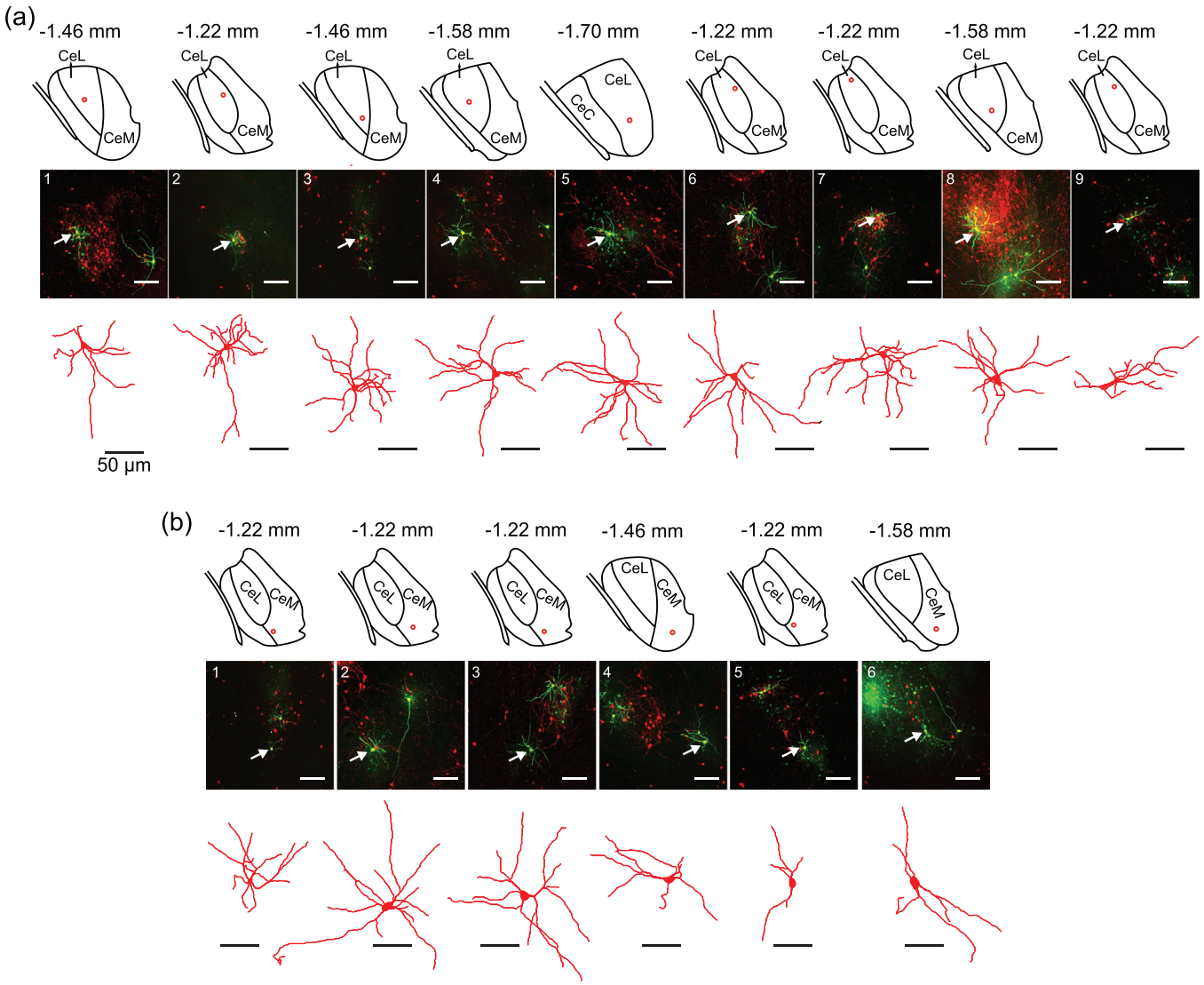

FIGURE 10 Morphology and anatomic location of recorded late-firing CRH+ neurons in CeL and CeM. Anatomical location (top), fluorescent image (middle), and morphological reconstruction (bottom) for late-firing CRH+ neurons recorded in CeL (a1–a9) and CeM (b1–b6). Image scale bars: 100 μm. Reconstruction scale bars: 50 μm

co-express CRH (Kim et al., 2017). Given that CeL-CRH+ neurons from this study displayed a late-firing phenotype, reported disparities in firing phenotypes of CeL-SOM neurons may be related to CRH co-expression. Another recent study showed that PKC-δ+ and SOM+ CeC/CeL neurons consisted of three intrinsically distinct phenotypes with different proportion, including late-firing, regular-firing, and spontaneous neurons (Adke et al., 2021). The neural type and proportion differences among these studies might be due to the different recording solutions (i.e., addition of excitatory and inhibitory synaptic blockers), ambiguity in the definition for the distinct CeA subregions, and differences in recording locations along the rostral–caudal axis in the CeA.

Robust expression of CRH+ neurons in the CeL with sparse expression in the CeM and CeC, respectively, is consistent with previous findings (Cassell et al., 1986; Li & Sheets, 2020; McCullough et al., 2018). However, sparse expression does not mean that the population is not functionally important. For example, it is reported that each memory engram is driven by a sparse population of neurons that are activated by a specific learning experience and undergo long-lasting synaptic modifications (Josselyn & Tonegawa, 2020; Sun et al., 2020). Our results suggest that future studies aimed at delineating the impact of CeA-CRH+ neurons on behavior or circuits need to consider functional differences of these neurons between substructures of the CeA. The ultimate outcome of such topographically nonspecific manipulation of CRH+ neurons in the entire CeA may mask distinct roles of CeL-CRH and CeM-CRH neurons. Moreover, functional variation of CRH+ neurons within the same or across different substructures of the CeA has not been fully resolved.

Numerous studies report diverse functional roles for CeA-CRH neurons. These include fear and anxiety (Asok et al., 2018; Dedic et al.,

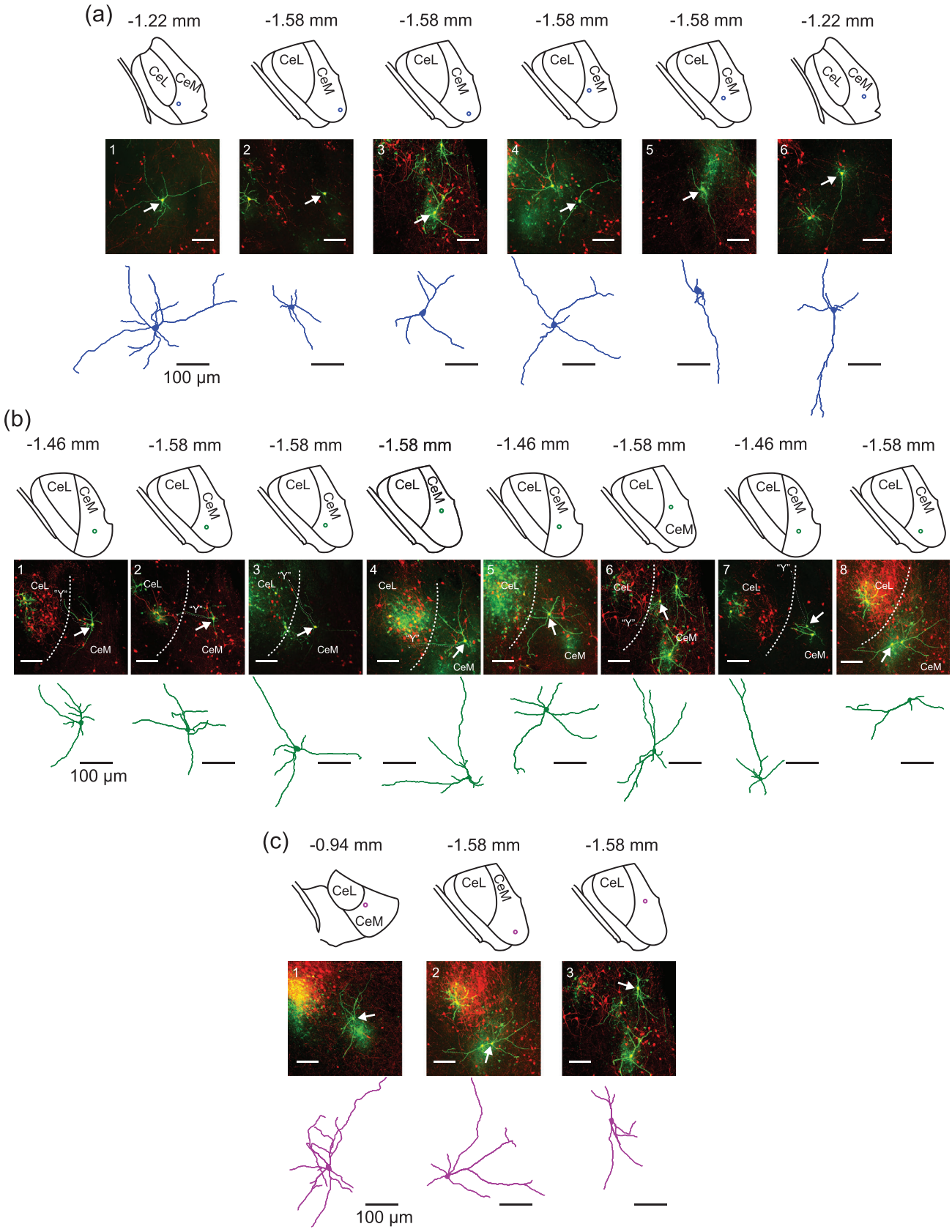

FIGURE 11 Morphology and anatomic location of recorded CeM-CRH+ neurons with distinct intrinsic phenotypes. Anatomical location (top), fluorescent image (middle), and morphological reconstruction (bottom) for regular-firing (a1–a6), bursting (b1–b8), and fast-spiking (c1–c3) CRH+ neurons in CeM. Dotted lines labeled "Y" in b1–b7 indicate dendrites of bursting CRH+ neurons reaching into the CeL. Image scale bars: 100 μm. Reconstruction scale bars: 100 μm

2018; McCall et al., 2015; Paretkar & Dimitrov, 2018; Pomrenze, Giovanetti, et al., 2019; Pomrenze, Tovar-Diaz, et al., 2019), learning in response to weak threats (Sanford et al., 2017), conditioned flight (Fadok et al., 2017), appetitive behaviors (Kim et al., 2017), alcohol dependence (de Guglielmo et al., 2019), and response to different pain modalities (Hein et al., 2021; Ji & Neugebauer, 2020; Li & Sheets, 2020). In addition, studies have demonstrated that neurons in the CeL and CeM are functionally different. For instance, neurons in the CeL are required for fear acquisition, while neurons in the CeM receive inhibitory input from the CeL and control fear expression (Ciocchi et al., 2010). Based on these findings, CRH+ neurons located in the CeL and CeM may present two functionally distinct neuronal populations involved in opposite, synergistic, or unrelated behaviors. Activating or inhibiting CRH+ neurons throughout both CeL and CeM may mask their respective roles. A good example is that bilateral inactivation of the entire CeA (CeM and CeL) did not elicit freezing behavior but rather inactivation of CeL alone or activation of CeM induced freezing responses (Ciocchi et al., 2010). Additional studies report functional heterogeneity within genetically defined neurons located in distinct substructures within brain regions (Bowen et al., 2020; Kim et al., 2017).

Topographically nonspecific targeting and cell-type-specific manipulation of CeA neurons cannot completely capture the functional heterogeneity within molecularly defined cell populations (Fadok et al., 2018; Li, 2019). Previous studies have attempted to establish the correlation between peptidergic neurons and neuronal morphology in rat (Cassell & Gray, 1989) and between molecular markers and firing phenotypes in mice (Douglass et al., 2017; Haubensak et al., 2010; Hunt et al., 2017; Li et al., 2013). Characterization using more complex, composite molecular, and/or anatomical identities has been proposed (Fadok et al., 2018). For example, CeA neurons expressing serotonin receptor 2a (Htr2a) were found to homogeneously exhibit late-firing properties and this population modulated food consumption, promoted positive reinforcement, and was active in vivo during eating. A previous study showed that PKC-δ+ neurons in the CeC and CeL have opposing functions in defensive behaviors (Kim et al., 2017), suggesting the functional heterogeneity within molecularly defined neurons is driven by location within distinct substructures of the CeA. Collectively, our intrinsic and morphological data suggest that CeL-CRH neurons are functionally homogeneous and CeM-CRH neurons are functionally diverse. However, whether intrinsic and morphological heterogeneity across CeA-CRH+ neurons are indicators of functional differences remains to be determined.

5 | CONCLUSIONS

This study demonstrated that a molecularly defined population of neurons across distinct subregions of the CeA display heterogeneous morphological and intrinsic phenotypes. While specific circuit and behavioral functions associated with these different phenotypes remain unclear, our findings contribute new insight for understanding the internal circuit organization and function of the CeA with a greater specificity. This work also supports the need to consider topographical and intrinsic heterogeneity within CeA neurons when interpreting findings from behavioral experiments where molecularly defined CeA neurons are being manipulated. Future work using a comprehensive approach with methods accounting for molecular markers, electrophysiology, morphology, and spatial location will improve our understanding of the highly complex cellular networks within the CeA.

ACKNOWLEDGMENTS

This work was funded by NIH grant R01-R01-NS112632. The graphical abstract was created using BioRender (Toronto, ON).

CONFLICT OF INTEREST

The authors declare no conflict of interest.

AUTHOR CONTRIBUTIONS

J.L. and P.L.S. designed research. J.L. and K.C. performed experiments. J.L. and P.L.S analyzed data. J.L., K.C., and P.L.S. wrote the paper.

DATA AVAILABILITY STATEMENT

The data sets supporting the current study have not been deposited in a public repository because all data collected are included in the study. Data are available from the corresponding author upon reasonable request.

PEER REVIEW

The peer review history for this article is available at https://publons.com/publon/10.1002/cne.25332.

ORCID

Patrick L. Sheets https://orcid.org/0000-0001-9630-2924

REFERENCES

Adke, A. P., Khan, A., Ahn, H. S., Becker, J. J., Wilson, T. D., Valdivia, S., Sugimura, Y. K., Martinez Gonzalez, S., & Carrasquillo, Y. (2021). Cell-type specificity of neuronal excitability and morphology in the central amygdala. *eNeuro*, *8*(1), ENEURO.0402–20.2020. https://doi.org/10.1523/ENEURO.0402-20.2020

Amano, T., Amir, A., Goswami, S., & Paré, D. (2012). Morphology, PKCδ expression, and synaptic responsiveness of different types of rat central lateral amygdala neurons. *Journal of Neurophysiology*, *108*(12), 3196–3205.

Asok, A., Draper, A., Hoffman, A. F., Schulkin, J., Lupica, C. R., & Rosen, J. B. (2018). Optogenetic silencing of a corticotropin-releasing factor pathway from the central amygdala to the bed nucleus of the stria terminalis disrupts sustained fear. *Molecular Psychiatry*, *23*(4), 914–922.

Bernard, J., Bester, H., & Besson, J. (1996). Involvement of the spino-parabrachio-amygdaloid and-hypothalamic pathways in the autonomic and affective emotional aspects of pain. *Progress in Brain Research*, *107*, 243–255.

Bernard, J. F., Alden, M., & Besson, J. M. (1993). The organization of the efferent projections from the pontine parabrachial area to the amygdaloid complex: A Phaseolus vulgaris leucoagglutinin (PHA-L) study in the rat. *Journal of Comparative Neurology*, *329*(2), 201–229.

Bowen, A. J., Chen, J. Y., Huang, Y. W., Baertsch, N. A., Park, S., & Palmiter, R. D. (2020). Dissociable control of unconditioned responses and associative fear learning by parabrachial CGRP neurons. *Elife*, *9*, e59799. https://doi.org/10.7554/eLife.59799

Callahan, L. B., Tschetter, K. E., & Ronan, P. J. (2013). Inhibition of corticotropin releasing factor expression in the central nucleus of the amygdala attenuates stress-induced behavioral and endocrine responses. *Frontiers in Neuroscience*, *7*, 195.

Cassell, M., & Gray, T. (1989). Morphology of peptide-immunoreactive neurons in the rat central nucleus of the amygdala. *Journal of Comparative Neurology*, *281*(2), 320–333.

Cassell, M., Gray, T., & Kiss, J. (1986). Neuronal architecture in the rat central nucleus of the amygdala: A cytological, hodological, and immunocytochemical study. *Journal of Comparative Neurology*, *246*(4), 478–499.

Cassell, M. D., Freedman, L. J., & Shi, C. (1999). The intrinsic organization of the central extended amygdala. *Annals of the New York Academy of Sciences*, *877*(1), 217–241.

Chiang, M. C., Nguyen, E. K., Canto-Bustos, M., Papale, A. E., Oswald, A. M., & Ross, S. E. (2020). Divergent neural pathways emanating from the lateral parabrachial nucleus mediate distinct components of the pain response. *Neuron*, *106*(6), 927–939. https://doi.org/10.1016/j.neuron.2020.03.014

Chieng, B. C., Christie, M. J., & Osborne, P. B. (2006). Characterization of neurons in the rat central nucleus of the amygdala: Cellular physiology, morphology, and opioid sensitivity. *Journal of Comparative Neurology*, *497*(6), 910–927.

Ciocchi, S., Herry, C., Grenier, F., Wolff, S. B., Letzkus, J. J., Vlachos, I., Ehrlich, I., Sprengel, R., Deisseroth, K., Müller, C., Lüthi, A., & Stadler, M. B. (2010). Encoding of conditioned fear in central amygdala inhibitory circuits. *Nature*, *468*(7321), 277–282.

de Guglielmo, G., Kallupi, M., Pomrenze, M. B., Crawford, E., Simpson, S., Schweitzer, P., Koob, G. F., Messing, R. O., & George, O. (2019). Inactivation of a CRF-dependent amygdalofugal pathway reverses addiction-like behaviors in alcohol-dependent rats. *Nature Communications*, *10*(1), 1238. https://doi.org/10.1038/s41467-019-09183-0

Dedic, N., Kühne, C., Jakovcevski, M., Hartmann, J., Genewsky, A. J., Gomes, K. S., Anderzhanova, E., Pöhlmann, M. L., Chang, S., Kolarz, A., Vogl, A. M., Dine, J., Metzger, M. W., Schmid, B., Almada, R. C., Ressler, K. J., Wotjak, C. T., Grinevich, V., Chen, A., … Kolarz, A. (2018). Chronic CRH depletion from GABAergic, long-range projection neurons in the extended amygdala reduces dopamine release and increases anxiety. *Nature Neuroscience*, *21*(6), 803–807.

Douglass, A. M., Kucukdereli, H., Ponserre, M., Markovic, M., Gründemann, J., Strobel, C., Alcala Morales, P. L., Conzelmann, K.-K., Lüthi, A., & Klein, R. (2017). Central amygdala circuits modulate food consumption through a positive-valence mechanism. *Nature Neuroscience*, *20*(10), 1384–1394.

Dumont, É. C., Martina, M., Samson, R. D., Drolet, G., & Paré, D. (2002). Physiological properties of central amygdala neurons: Species differences. *European Journal of Neuroscience*, *15*(3), 545–552.

Duvarci, S., & Pare, D. (2014). Amygdala microcircuits controlling learned fear. *Neuron*, *82*(5), 966–980.

Fadok, J. P., Krabbe, S., Markovic, M., Courtin, J., Xu, C., Massi, L., Botta, P., Bylund, K., Müller, C., Tovote, P., Lüthi, A., & Kovacevic, A. (2017). A competitive inhibitory circuit for selection of active and passive fear responses. *Nature*, *542*(7639), 96–100.

Fadok, J. P., Markovic, M., Tovote, P., & Lüthi, A. (2018). New perspectives on central amygdala function. *Current Opinion in Neurobiology*, *49*, 141–147.

Fulwiler, C. E., & Saper, C. B. (1984). Subnuclear organization of the efferent connections of the parabrachial nucleus in the rat. *Brain Research Reviews*, *7*(3), 229–259.

Gauriau, C., & Bernard, J.-F. (2002). Pain pathways and parabrachial circuits in the rat. *Experimental Physiology*, *87*(2), 251–258.

Hartley, N. D., Gaulden, A. D., Baldi, R., Winters, N. D., Salimando, G. J., Rosas-Vidal, L. E., Jameson, A., Winder, D. G., & Patel, S. (2019). Dynamic remodeling of a basolateral-to-central amygdala glutamatergic circuit across fear states. *Nature Neuroscience*, *22*(12), 2000–2012. https://doi.org/10.1038/s41593-019-0528-7

Haubensak, W., Kunwar, P. S., Cai, H., Ciocchi, S., Wall, N. R., Ponnusamy, R., Biag, J., Dong, H.-W., Deisseroth, K., Fanselow, M. S., Lüthi, A., Anderson, D. J., & Callaway, E. M. (2010). Genetic dissection of an amygdala microcircuit that gates conditioned fear. *Nature*, *468*(7321), 270–276.

Hein, M., Ji, G., Tidwell, D., D'Souza, P., Kiritoshi, T., Yakhnitsa, V., Navratilova, E., Porreca, F., & Neugebauer, V. (2021). Kappa opioid receptor activation in the amygdala disinhibits CRF neurons to generate pain-like behaviors. *Neuropharmacology*, *185*, 108456. https://doi.org/10.1016/j.neuropharm.2021.108456

Herman, J. P., McKlveen, J. M., Ghosal, S., Kopp, B., Wulsin, A., Makinson, R., Scheimann, J., & Myers, B. (2011). Regulation of the hypothalamic-pituitary-adrenocortical stress response. *Comprehensive Physiology*, *6*(2), 603–621.

Hunt, S., Sun, Y., Kucukdereli, H., Klein, R., & Sah, P. (2017). Intrinsic circuits in the lateral central amygdala. *eNeuro*, *4*(1), ENEURO.0367–16.2017. https://doi.org/10.1523/ENEURO.0367-16.2017

Janak, P. H., & Tye, K. M. (2015). From circuits to behaviour in the amygdala. *Nature*, *517*(7534), 284–292.

Jhamandas, J. H., Petrov, T., Harris, K. H., Vu, T., & Krukoff, T. L. (1996). Parabrachial nucleus projection to the amygdala in the rat: Electrophysiological and anatomical observations. *Brain Research Bulletin*, *39*(2), 115–126.

Ji, G., & Neugebauer, V. (2020). Kappa opioid receptors in the central amygdala modulate spinal nociceptive processing through an action on amygdala CRF neurons. *Molecular Brain*, *13*(1), 128. https://doi.org/10.1186/s13041-020-00669-3

Jolkkonen, E., & Pitkanen, A. (1998). Intrinsic connections of the rat amygdaloid complex: Projections originating in the central nucleus. *Journal of Comparative Neurology*, *395*(1), 53–72.

Joseph, S. A., & Knigge, K. M. (1983). Corticotropin releasing factor: Immunocytochemical localization in rat brain. *Neuroscience Letters*, *35*(2), 135–141.

Josselyn, S. A., & Tonegawa, S. (2020). Memory engrams: Recalling the past and imagining the future. *Science*, *367*(6473), eaaw4325. https://doi.org/10.1126/science.aaw4325

Keifer, O. P., Jr., Hurt, R. C., Ressler, K. J., & Marvar, P. J. (2015). The physiology of fear: Reconceptualizing the role of the central amygdala in fear learning. *Physiology*, *30*(5), 389–401.

Kim, J., Zhang, X., Muralidhar, S., LeBlanc, S. A., & Tonegawa, S. (2017). Basolateral to central amygdala neural circuits for appetitive behaviors. *Neuron*, *93*(6), 1464.e5–1479.e5.

Kiritoshi, T., & Neugebauer, V. (2018). Pathway-specific alterations of cortico-amygdala transmission in an arthritis pain model. *ACS Chemical Neuroscience*, *9*(9), 2252–2261.

Li, B. (2019). Central amygdala cells for learning and expressing aversive emotional memories. *Current Opinion in Behavioral Sciences*, *26*, 40–45.

Li, H., Penzo, M. A., Taniguchi, H., Kopec, C. D., Huang, Z. J., & Li, B. (2013). Experience-dependent modification of a central amygdala fear circuit. *Nature Neuroscience*, *16*(3), 332–339.

Li, J. N., & Sheets, P. L. (2018). The central amygdala to periaqueductal gray pathway comprises intrinsically distinct neurons differentially affected in a model of inflammatory pain. *The Journal of Physiology*, *596*(24), 6289–6305.

Li, J. N., & Sheets, P. L. (2020). Spared nerve injury differentially alters parabrachial monosynaptic excitatory inputs to molecularly specific neurons in distinct subregions of the central amygdala. *Pain*, *161*(1), 166–176. https://doi.org/10.1097/j.pain.0000000000001691

Marek, R., Strobel, C., Bredy, T. W., & Sah, P. (2013). The amygdala and medial prefrontal cortex: Partners in the fear circuit. *Journal of Physiology*, *591*(Pt 10), 2381–2391. https://doi.org/10.1113/jphysiol.2012.248575

Martina, M., Royer, S., & Paré, D. (1999). Physiological properties of central medial and central lateral amygdala neurons. *Journal of Neurophysiology*, *82*(4), 1843–1854.

McCall, J. G., Al-Hasani, R., Siuda, E. R., Hong, D. Y., Norris, A. J., Ford, C. P., & Bruchas, M. R. (2015). CRH engagement of the locus coeruleus noradrenergic system mediates stress-induced anxiety. *Neuron*, *87*(3), 605–620.

McCullough, K. M., Morrison, F. G., Hartmann, J., Carlezon, W. A., Jr., & Ressler, K. J. (2018). Quantified coexpression analysis of central amygdala subpopulations. *Eneuro*, *5*(1), ENEURO.0010–18.2018.

McDonald, A. J. (1982). Cytoarchitecture of the central amygdaloid nucleus of the rat. *Journal of Comparative Neurology*, *208*(4), 401–418.

Mork, B. E., Lamerand, S. R., Zhou, S., Taylor, B. K., & Sheets, P. L. (2022). Sphingosine-1-phosphate receptor 1 agonist SEW2871 alters membrane properties of late-firing somatostatin expressing neurons in the central lateral amygdala. *Neuropharmacology*, *203*, 108885. https://doi.org/10.1016/j.neuropharm.2021.108885

Nagase, M., Mikami, K., & Watabe, A. M. (2019). Parabrachial-to-amygdala control of aversive learning. *Current Opinion in Behavioral Sciences*, *26*, 18–24.

Neugebauer, V. (2015). Amygdala pain mechanisms. In H. G. Schaible (Ed.), *Pain control* (pp. 261–284). Springer.

Neugebauer, V., Li, W., Bird, G. C., & Han, J. S. (2004). The amygdala and persistent pain. *The Neuroscientist*, *10*(3), 221–234. https://doi.org/10.1177/1073858403261077

Pape, H.-C., & Pare, D. (2010). Plastic synaptic networks of the amygdala for the acquisition, expression, and extinction of conditioned fear. *Physiological Reviews*, *90*(2), 419–463.

Paretkar, T., & Dimitrov, E. (2018). The central amygdala corticotropin-releasing hormone (CRH) neurons modulation of anxiety-like behavior and hippocampus-dependent memory in mice. *Neuroscience*, *390*, 187–197.

Pomrenze, M. B., Giovanetti, S. M., Maiya, R., Gordon, A. G., Kreeger, L. J., & Messing, R. O. (2019). Dissecting the roles of GABA and neuropeptides from rat central amygdala CRF neurons in anxiety and fear learning. *Cell Reports*, *29*(1), 13.e4–21.e4.

Pomrenze, M. B., Tovar-Diaz, J., Blasio, A., Maiya, R., Giovanetti, S. M., Lei, K., Morikawa, H., Hopf, F. W., & Messing, R. O. (2019). A corticotropin releasing factor network in the extended amygdala for anxiety. *Journal of Neuroscience*, *39*(6), 1030–1043.

Sanford, C. A., Soden, M. E., Baird, M. A., Miller, S. M., Schulkin, J., Palmiter, R. D., Clark, M., & Zweifel, L. S. (2017). A central amygdala CRF circuit facilitates learning about weak threats. *Neuron*, *93*(1), 164–178.

Saper, C., & Loewy, A. (1980). Efferent connections of the parabrachial nucleus in the rat. *Brain Research*, *197*(2), 291–317.

Sarhan, M., Freund-Mercier, M. J., & Veinante, P. (2005). Branching patterns of parabrachial neurons projecting to the central extended amygdala: Single axonal reconstructions. *Journal of Comparative Neurology*, *491*(4), 418–442.

Schiess, M. C., Callahan, P. M., & Zheng, H. (1999). Characterization of the electrophysiological and morphological properties of rat central amygdala neurons in vitro. *Journal of Neuroscience Research*, *58*(5), 663–673.

Sun, N., & Cassell, M. D. (1993). Intrinsic GABAergic neurons in the rat central extended amygdala. *Journal of Comparative Neurology*, *330*(3), 381–404.

Sun, X., Bernstein, M. J., Meng, M., Rao, S., Sorensen, A. T., Yao, L., Zhang, X., Anikeeva, P. O., & Lin, Y. (2020). Functionally distinct neuronal ensembles within the memory engram. *Cell*, *181*(2), 410.e17–423.e17. https://doi.org/10.1016/j.cell.2020.02.055

Thompson, J. M., & Neugebauer, V. (2017). Amygdala plasticity and pain. *Pain Research and Management*, *2017*, 8296501.

Tokita, K., Inoue, T., & Boughter, J. D., Jr. (2010). Subnuclear organization of parabrachial efferents to the thalamus, amygdala and lateral hypothalamus in C57BL/6J mice: A quantitative retrograde double labeling study. *Neuroscience*, *171*(1), 351–365.

Wang, S., Tanzi, R. E., & Li, A. (2019). Quantitative analysis of neuronal dendritic arborization complexity in *Drosophila*. *The Journal of Visualized Experiments*, , . https://doi.org/10.3791/57139

How to cite this article: Li, J.-N., Chen, K., & Sheets, P. L. (2022). Topographic organization underlies intrinsic and morphological heterogeneity of central amygdala neurons expressing corticotropin-releasing hormone. *Journal of Comparative Neurology*, *530*, 2286–2303. https://doi.org/10.1002/cne.25332